Kernel-based Atlas Image Selection for Brain Tissue Segmentation

Cárdenas-Peña, D.* and Orbes-Arteaga, M.* and Castellanos-Dominguez, G.*

***Abstract*— We propose a new Kernel-based Atlas Image Selection computed in the Embedding Representation space (termed KAISER) aiming to support labeling of brain tissue on 3D magnetic resonance (MR) images. KAISER approach provides efficient feature extraction from MR volumes based on an introduced inter-slice kernel (ISK). Thus, using the ISK matrix eigendecomposition, the inherent structure of data distribution is accentuated through estimation of low dimensional compact space where every pair-wise image similarity can be better measured. We compare our proposal against the whole-population atlas, randomly and demographically selected multi-atlas approaches in a four-tissue image labeling task. Obtained results show that the KAISER approach outperforms other alternative techniques (98% Dice index similarity against 94%), while exhibiting better repeatability.**

I. INTRODUCTION

Magnetic Resonance (MR) images are used in many medical applications, by instance, to model evolution of pathologies (like Alzheimer, dementia or schizophrenia) by estimating anatomical or functional structure changes through time or space. Also, MR information benefits structural model estimation of head conductivity patterns required for electromagnetic source reconstruction algorithms [1]. Nonetheless, either application requires an accurate brain structure segmentation that is a somewhat complicated task, mainly, due to the low inter-structure contrast and image artifacts [2]. Hence, spatial functions (termed as atlas or templates) have been proposed for modeling head structure distribution. To this end, templates are provided as sets of shape, intensity and/or functional models [3]. However, performance of the atlas-based segmentation highly depends on the carried out template-to-image registration [4].

Although unimodal shape distributions may be assumed, accomplished solutions are mostly biased since atlases are computed from anatomically unrepresentative images [1]. In contrast, the multi-atlas segmentation schemes are more efficient when more representative atlases can be estimated from large datasets. Besides, as discussed in [4], atlas construction can take into account particular aspects of image similarity like demographic affinity among subjects as in [1]. Nevertheless, most of the demographic-based approaches assume that image distributions depend only on few considered grouping categories (e.g. age and gender), but at the same time they neglect the influence of others (e.g. disease or handedness). Moreover, to take into account all possible demographic groups is a not tractable task.

On the other hand, atlas construction is usually based on information measures that are time-consuming, especially, in cases of many images. Distance pre-computation approaches attempt to cope with this issue. Thus, in [5], three manifold learning techniques are discussed for computing compact spaces where images are compared. Comparison of a new query against the dataset is estimated as accumulation of the atlas-image-to-single-template and single-template-to-query-image measures; This aspect may lead to a suboptimal selection, given that the employed measure is not guaranteed to match all distance properties. Another approach in [6] estimates atlas functions from an offline-computed image cluster. A new query image is assigned to one of resulting groups using a similarity index between the average cluster segmentation and a query image pre-segmentation, calculated using the whole-population atlas. However, performance depends not only on the size and number of clusters, but also on the resulting pre-segmentation, which can be already biased by the whole-population atlas.

For supporting brain tissue segmentation, we propose a new Kernel-based Atlas Image Selection, computed in the Embedding Representation space (termed KAISER), that projects all dataset images into a compact eigendecomposition-based space. In such space, regular distances can be more accurately calculated, due to its low dimensionality, and latent data structure is highlighted. The KAISER approach is compared against the whole-population atlas and conventional demographic multi-atlas selection on a four tissue image labeling task. Results suggest that our approach outperforms other methods used in this work in both, average performance and repeatability.

II. BACKGROUND

A. Bayesian medical image segmentation

As proposed in [3], [7], automatic labeling of medical images can be stated within a Bayesian classification framework as estimation of a label set, $\mathcal{L}=\{l_r\in[1,C]:r\in\Omega\}$, from a given set of measurements (or *image*), $\mathcal{I}=\{\boldsymbol{x}_r\in\mathbb{R}^d\}$, where a single label, l_r, is assigned to the r-th spatial element (or *spel*), depending on the d-dimensional measurement vector $\boldsymbol{x}_r$, where $C\in\mathbb{N}$ is the total number of considered labels or classes, and Ω is the spel domain.

In the Bayesian framework, provided a given query image, the probability of having a label set, $P(\mathcal{L}|\mathcal{I})$, the probability of occurring the image given the labeling, $P(\mathcal{I}|\mathcal{L})$, and the

*Universidad Nacional de Colombia, Sede Manizales, La Nubia, Colombia, Signal Processing and Recognition Group. {dcardenasp,morbesa,cgcastellanosd}@unal.edu.co

This work was supported by *Programa Nacional de Formación de Investigadores "Generación del Bicentenario"*, 2011/2012, *Programa Nacional de Jóvenes investigadores e innovadores*, 2012, and the research project 111056934461, all funded by COLCIENCIAS.

978-1-4244-7929-0/14/$26.00 ©2014 IEEE

label prior probability, $P(\mathcal{L})$, are together related as:

$$P(\mathcal{L}|\mathcal{I}) \propto P(\mathcal{I}|\mathcal{L})P(\mathcal{L}) \quad (1)$$

In most of medical imaging applications, measurement vector distributions of different tissues are overlapped. Consequently, the probabilities $P(\mathcal{I}|\mathcal{L})$ and $P(\mathcal{L})$ (termed *atlas functions*), can vary spatially, so that a set of Bayesian classifiers is applied along Ω, where each one deals with independent small regions. Hence, the probability of obtaining a label set given a query image is represented as $P(\mathcal{L}|\mathcal{I}) = \prod_{r\in\Omega} P(l_r = c|\boldsymbol{x}_r)$, where $P(l_r = c|\boldsymbol{x}_r) = P(\boldsymbol{x}_r|l_r{=}c)P(l_r)/P(\boldsymbol{x}_r)$ is the probability of obtaining the label $c \in [1, C]$ at spel r and given the measurement $\boldsymbol{x}_r$, $P(\boldsymbol{x}_r|l_r{=}c)$ is the conditional probability of observing the measurement $\boldsymbol{x}_r$ at r given the label $l_r = c$, $P(l_r)$ is the label prior probability, and $P(\boldsymbol{x}_r)$ is the evidence probability.

B. Learning model parameters

Therefore, the segmentation task relies on estimation of the atlas functions from a given set of N pre-labeled atlas images, $\mathcal{X} = \{\mathcal{I}_n, \mathcal{L}_n\}$, where the r-th spel of the n-th image is assigned to the measurement vector $\boldsymbol{x}_r^n$ and the class l_r^n. Hence, provided $\mathcal{X}$, the prior $P(l_r = c)$ and evidence $P(\boldsymbol{x}_r)$, both the atlas functions can be computed as:

$$P(l_r = c) = \boldsymbol{E}\{\delta(l_r^n - c) : \forall n \in N\} \quad (2a)$$

$$P(\boldsymbol{x}_r) = \sum\nolimits_{c\in C} P(\boldsymbol{x}_r|l_r = c)P(l_r = c) \quad (2b)$$

where $\delta(\cdot)$ is the delta function and notation $\boldsymbol{E}\{\cdot\}$ stands for the expectation operator.

In each class, $\boldsymbol{x}_r$ is assumed to be normally distributed [7], $\boldsymbol{x} \sim \mathcal{N}(\boldsymbol{\mu}_r^c, \boldsymbol{\Sigma}_r^c)$, where mean $\boldsymbol{\mu}_r^c \in \mathbb{R}^d$ and covariance $\boldsymbol{\Sigma}_r^c \in \mathbb{R}^{d\times d}$ class parameters are estimated as:

$$\boldsymbol{\mu}_r^c = \boldsymbol{E}\{\boldsymbol{x}_r^n | l_r^n = c : \forall n \in N\} \quad (3a)$$

$$\boldsymbol{\Sigma}_r^c = \boldsymbol{E}\{(\boldsymbol{x}_r^n - \boldsymbol{\mu}_r^c)(\boldsymbol{x}_r^n - \boldsymbol{\mu}_r^c)^\top | l_r^n = c : \forall n \in N\}, \quad (3b)$$

Since the N-image set is mostly heterogeneous, some objects can bias the segmentation obtained over a given query image. Hence, we propose to enhance the above explained approach by computing the atlas functions for a given subject from a subpopulation of the entire dataset, which in turn depends on a new introduced pair-wise image similarity.

C. Image Similarity Measure

In order to encode the affinity between a couple of images, $\{\mathcal{I}_n, \mathcal{I}_m\}$, from a given image set $\mathcal{X}$, we introduce the following kernel function:

$$\zeta(\mathcal{I}_n, \mathcal{I}_m) = \langle \varphi(\mathcal{I}_n), \varphi(\mathcal{I}_m) \rangle \quad (4)$$

where $\varphi(\cdot)$ maps from the original domain, Ω, into a Reproduced Kernel Hilbert Space $\mathcal{H}$. Notation $\langle\cdot,\cdot\rangle$ stands for the inner product. Generally, it holds that $|\mathcal{H}| \to \infty$, so that $|\Omega| \ll |\mathcal{H}|$ can be assumed. Nevertheless, there is no need for computing $\varphi(\cdot)$ directly. Instead, the well-known *kernel trick* is employed for computing the elements of the matrix $\boldsymbol{Z} \in \mathbb{R}^{N\times N}$ encoding pair-wise image similarities. The matrix $\boldsymbol{Z}$ is estimated from the set $\mathcal{X}$ and holding elements $z_{nm} = \zeta(\mathcal{I}_n, \mathcal{I}_m)$ with $z_{nm} \in \mathbb{R}^+$.

Aiming to minimize redundant information, we se the well-known common principal components analysis (PCA) that decomposes the similarity matrix as: $\boldsymbol{Z} = \boldsymbol{V}\boldsymbol{\Lambda}\boldsymbol{V}^\top$, where $\boldsymbol{\Lambda} \in \mathbb{R}^{N\times N}$ is a diagonal matrix containing the ranked in descending-order eigenvalues of $\boldsymbol{Z}$ and matrix $\boldsymbol{V} \in \mathbb{R}^{N\times N}$ holds its column eigenvectors. In this sense, to represent $\mathcal{I}_n$ we use a vector $\boldsymbol{u}_n \in \mathbb{R}^p$ obtained as: $\boldsymbol{u}_n = \sum_{m\in N} z_{nm}\tilde{\boldsymbol{v}}_m$, where $\tilde{\boldsymbol{v}}_m$ is the m-th column of $\boldsymbol{V}$ truncated to the p most relevant components in terms of its corresponding eigenvalue.

D. Image Feature Extraction

Here, the original spatial domain specifically corresponds to $\Omega = \mathbb{R}^{W\times H\times L}$, so that any spel is an index triplet in the form: $r = (i, j, k)$, with $i \in [1, W], j \in [1, H], k \in [1, L]$. Thus, each image can be arranged as an ordered slice set $\mathcal{I} = \{\boldsymbol{S}_k : k \in [1, L]\}$, being $\boldsymbol{S}_k = \{\boldsymbol{x}_r : r = (i, j, k)\}$, with $\boldsymbol{S}_k \in \mathbb{R}^{W\times H}$ the k-th $(W \times H)$-sized matrix slice.

Assuming smooth variations between adjacent slices on $\mathcal{I}$, inter-slice relationship is encoded by the kernel function: $\gamma(\boldsymbol{S}_k, \boldsymbol{S}_{k'}) = \langle \varphi(\boldsymbol{S}_k), \varphi(\boldsymbol{S}_{k'}) \rangle$. Thus, the output symmetric matrix $\boldsymbol{G} \in \mathbb{R}^{L\times L}$ with real-valued elements, $g_{kk'} = \gamma(\boldsymbol{S}_k, \boldsymbol{S}_{k'})$, becomes the inter-slice kernel (ISK) of $\mathcal{I}$. Moreover, provided $g_{kk'} = g_{k'k}$ and $g_{kk} = 1$, each image $\mathcal{I}_n$ can be represented by the upper triangular ISK elements as a vector $\boldsymbol{y}_n \in \mathbb{R}^{L(L-1)/2}$. Therefore, the image similarity measure in Eq. (4) is represented as: $\zeta(\mathcal{I}_n, \mathcal{I}_m) = f(\boldsymbol{y}_n, \boldsymbol{y}_m)$, where $f(\cdot,\cdot)$ is the introduced kernel function.

III. EXPERIMENTAL SETUP

A. Database

The `OASIS` dataset is a brain imaging study, holding an MR image collection from 416 subjects, aged 18 to 96 years old, including diagnosed very mild dementia (70), mild dementia (28), moderate dementia (2), and healthy (316) subjects. For each of them, three or four T1-weighted MR scans obtained within a single imaging session are included (see a sample subject in Fig. 1), from which a motion-corrected co-registered average image is obtained. Additionally, each subject is provided with ground-truth segmented gray matter (GM), white matter (WM) and cerebro-spinal fluid (CSF) structures. A fourth label (BG) is included in the present study, aiming to model the background of images, as the regions with no provided label.

B. Preprocessing

In order to enable comparisons between patient-dependent atlas and a whole-population atlas, alignment and intensity normalization are performed as preprocessing steps, as opposed to [3], [7] where both steps are included in the Bayesian framework. For alignment, each image is registered to the MNI305 template by an affine transformation so that the whole dataset is referenced to the Talairach space and resampled to match the template size ($W{=}197, H{=}233, L{=}189$). Then, the intensity normalization procedure is carried

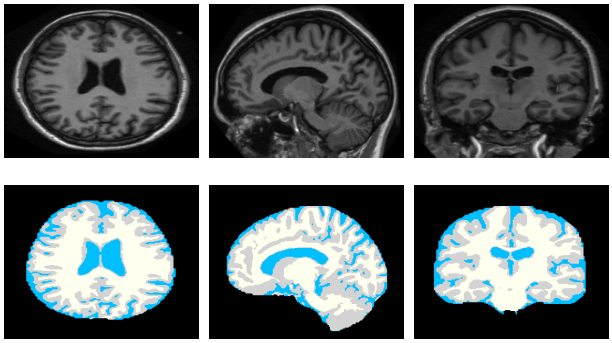

Fig. 1. Sample subject of the OASIS dataset publicly available in `http://www.oasis-brains.org`. Top row: Motion corrected MR image. Bottom row: Provided structure segmentation. Left to right: Axial, Sagittal and Coronal axes.

out by scaling each spel value so that the average intensity of the white matter is the same in all MRIs.

C. Proposed Image Feature Extraction

We note the ISK of a given image as $\boldsymbol{y}_n \in \mathbb{R}^{L(L-1)/2}$. Hence, a new representation space of order 10^4 is achieved, instead of the original image domain of order 10^6. Specifically, to compute $\gamma_{kk'}$ of each image, we use the Gaussian kernel $\gamma\left(\boldsymbol{S}_k, \boldsymbol{S}_{k'}\right) = \exp\left(-||\mathbf{S}_k - \mathbf{S}_{k'}||_F^2/(2\sigma_\kappa^2)\right)$, where $\sigma_\kappa \in \mathbb{R}^+$ is a scale parameter and notation $\|\cdot\|_F$ stands for the Frobenius norm. Since an appropriate σ_κ value spans widely the values of $\boldsymbol{G}$ and taking into account that $\lim_{\sigma_k \to 0} \text{Var}(\boldsymbol{G}(\sigma_k)) = 0$, $\lim_{\sigma_k \to \infty} \text{Var}(\boldsymbol{G}(\sigma_k)) = 0$, optimization of the scale parameter is performed by maximizing the following element-wise matrix variance:

$$\sigma_\kappa^* = \arg\max_{\sigma} \left\{\text{Var}\{\boldsymbol{\gamma}_{kk'}(\sigma) : \forall k \neq k'\}\right\}, \qquad (5)$$

Fig. 2 shows resulting tuning sagittal ISK curve, where the mean and standard deviation values are computed from the whole set of MR images.

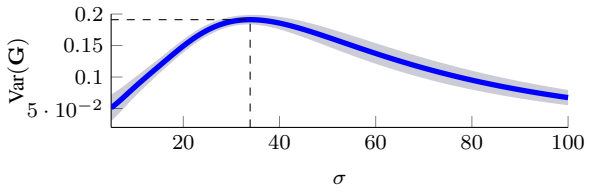

Fig. 2. Scale parameter vs. kernel element-wise variance for the sagittal ISK. Mean and standard deviation values are plotted.

D. Kernel-based Image Similarity

Given the aforementioned image feature extraction, a new low-dimensional, compact space is built from the ISK representation by using, in the Eq. (4), the well-known Gaussian kernel on each image's ISK: $\zeta(\mathcal{I}_n, \mathcal{I}_m) = \exp\left(-\|\boldsymbol{y}_n - \boldsymbol{y}_m\|_2^2/(2\sigma_\zeta^2)\right)$, where notation $\|\cdot\|_2$ stands for the Euclidean norm and the scale $\sigma_\zeta \in \mathbb{R}^+$ is tuned as in Eq. (5). A scale of $\sigma_\zeta = 9$ is obtained using the above proposed tuning procedure. The resulting kernel is depicted in Fig. 3(a), where each row and column represents a given image on the dataset. Images are ordered by gender (firstly) and age (secondly).

Therefore, the PCA-based projection space is computed from kernel $\boldsymbol{Z}$. As seen in Fig. 3(b) showing the four largest decomposition eigenvectors, there exists an inherent structure, hidden on the image distribution, that is hard to identify in the original space domain (Ω), but easily identifiable in the proposed projected space. As a result, patient-dependent atlases lead to more accurate segmentation results than the whole-population atlas.

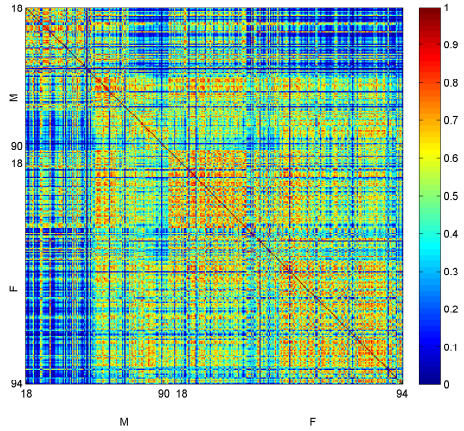

(a) Kernel matrix using the ISK features

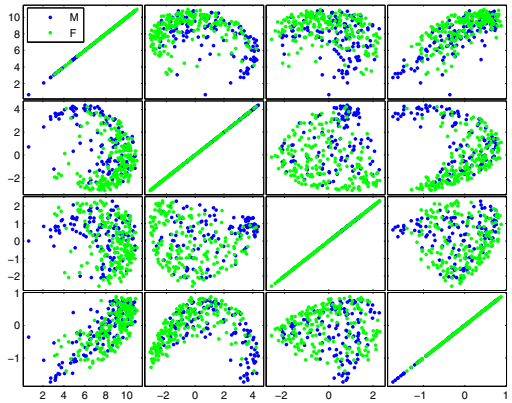

(b) Data projection along the first four eigenvectors

Fig. 3. Kernel matrix (top) and eigen-projection (bottom) representations for the OASIS dataset.

Finally, the well-known L-curve criterion is used to tune the value p to truncate the number of components employed on the projected representation $\boldsymbol{v} \in \mathbb{R}^p$. For such criterion, the minimum distance to origin from a curve, composed by the normalized eigenvalues and the percentage of components, has to be found. For the OASIS dataset, such distance is found at the ninth component. Hence, subsequent analyses are performed with $p = 9$.

E. Tissue Labeling Performance

Taking into account the image similarity measure described in Section II-C, we propose four strategies for choosing the image subset used for computation of the

atlas functions: *i)* using the whole dataset on the Bayesian Classification Framework (FULL) [3], as a state-of-the-art comparative baseline; *ii)* extracting N_k samples using the proposed **K**ernel-based **A**tlas **I**mage **S**election from the **E**mbedding **R**epresentation, termed KAISER; *iii)* randomly choosing a subset of N_r images (RAND), as the comparative approach used in [4], with $N_r = 20$ and 10 folds. *iv)* Selecting demographically affine images to the query image (DEMG), using gender and age categories, as in [1].

For measuring segmentation quality of above described approaches, we assess agreement between resulting segmentations and the labels provided for each dataset image. Namely, we employ the Dice index: $d = 2|\mathcal{A} \cap \mathcal{B}|/(|\mathcal{A}|+|\mathcal{B}|)$, where $\mathcal{A}$ and $\mathcal{B}$ are respectively the provided and estimated regions of the compared tissue, and $|\cdot|$ stands for the number of spels on a given region. Additionally, to prove the repeatability of the approaches, a leave-one-out (LOO) cross-validation scheme is employed. Specifically for KAISER, the number of neighbors N_k has to be tuned; this procedure is done by intensive searching of the largest average-accuracy-over-standard-deviation ratio in the LOO scheme. Search is performed over the interval $N_k = [5, 21]$, as shown in Fig. 4, where the optimum value is found at $N_k = 13$ neighbors.

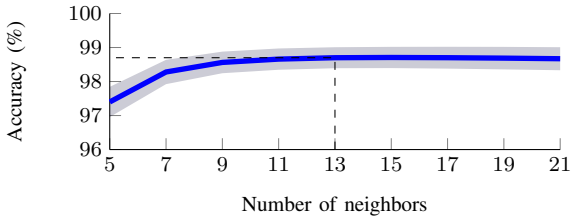

Fig. 4. Overall accuracy segmentation versus the number of selected closest neighbors for the proposed KAISER. Errorbar is displayed for a LOO validation scheme.

Once tuned the number of neighbors, the Dice index and overall accuracy are computed for the compared approaches in the LOO validation scheme. Mean and standard deviation results, provided in Table I, show that proposed KAISER outperforms FULL on all items.

TABLE I

SEGMENTATION RESULTS FOR CONSIDERED SELECTION APPROACHES

	BG	*WM*	*GM*	*CSF*	*Acc*
FULL [3]	100	81.5 ± 8.8	85.8 ± 5.4	84.5 ± 7.6	96.1 ± 1.4
KAISER	100	92.1 ± 1.9	95.1 ± 1.4	96.2 ± 1.0	98.7 ± 0.3
RAND [4]	100	74.6 ± 6.7	81.7 ± 5.1	79.2 ± 7.0	94.8 ± 1.3
DEMG [1]	100	77.2 ± 5.9	83.6 ± 5.7	82.2 ± 6.7	95.4 ± 1.4

IV. DISCUSSION AND CONCLUDING REMARKS

Here, a new atlas selection strategy for supporting brain tissue segmentation is proposed based on an image similarity measure computed on a low dimensional representation space, resulting in two main contributions: Firstly, a new inter-slice-kernel-based image feature extraction is recommended, where the relationships along a given image axis are encoded. Secondly, a KPCA-based projection space is computed from the ISK representation so that the inherent structure of the data distribution is highlighted. Such contributions allowed the proposed approach to outperform the baseline (FULL) and demographic atlas-based (DEMG) approaches, at least 10%, while proving that the selection of the subset is better than a randomly chosen one (RAND). Also, from obtained results, the following comments arise:

Regarding the scale parameter for the ISK feature extraction, an stable measure can be seen on Fig. 2, leading us to conclude that such kind of parameter tuning is a suitable approach for large datasets. Nevertheless, its benefit has to be proved on other machine learning tasks and kinds of data.

The computed pairwise image kernel, shown in Fig. 3(a) and sorted by gender (firstly) and age (secondly), shows a stacked-block-like shape, leading to infer that there are relationships clustering demographic groups. Later, the KPCA-based projection, provided in Fig. 3(b), proved that, in fact, there is a hidden data distribution structure due to the non-linear relationship among the eigenvectors.

Overall, obtained segmentation results (see Table I) show that the KAISER proposal achieved the largest average and the least deviation values for all Dice indexes and accuracy. Hence, our proposal exhibits the best classification performance and the most repeatability. The above leads to an improvement, regarding the atlas selection, on multi-atlas-based image labeling approaches.

As future work, three main research lines are proposed. *i*) Since obtained decomposition eigenvectors showed non-linear relationships, other non-linear embedding techniques, e.g. Laplacian eigenmaps and local linear embedding, can be used for highlighting the essential structure. *ii*) A future research field is to prove the ability of the proposal in more complex structure labeling tasks, such as subcortical segmentation. *iii*) Finally, new feature extraction methodologies based on mixing ISK along the three main axes can be explored, aiming encode all dynamics into shorter and more compact versions of the MR volumes.

REFERENCES

[1] P. a. Valdés-Hernández, N. von Ellenrieder, A. Ojeda-Gonzalez, S. Kochen, Y. Alemán-Gómez, C. Muravchik, and P. a. Valdés-Sosa, "Approximate average head models for EEG source imaging." *Journal of neuroscience methods*, vol. 185, no. 1, pp. 125–32, Dec. 2009.

[2] D. Cardenas-Pena, J. D. Martinez-Vargas, and G. Castellanos-Dominguez, "Local binary fitting energy solution by graph cuts for MRI segmentation." *Conf Proc IEEE Eng Med Biol Soc.*, vol. 2013, no. 2, pp. 5131–4, Jan. 2013.

[3] J. Ashburner and K. J. Friston, "Unified segmentation." *NeuroImage*, vol. 26, no. 3, pp. 839–51, Jul. 2005.

[4] P. Aljabar, R. a. Heckemann, a. Hammers, J. V. Hajnal, and D. Rueckert, "Multi-atlas based segmentation of brain images: atlas selection and its effect on accuracy." *NeuroImage*, vol. 46, no. 3, pp. 726–38, Jul. 2009.

[5] A. K. Hoang Duc, M. Modat, K. K. Leung, J. Barnes, T. Kadir, and S. Ourselin, "Using manifold learning for atlas selection in multi-atlas segmentation." *PloS one*, vol. 8, no. 8, p. e70059, Jan. 2013.

[6] T. R. Langerak, F. F. Berendsen, U. a. Van der Heide, A. N. T. J. Kotte, and J. P. W. Pluim, "Multiatlas-based segmentation with preregistration atlas selection." *Medical physics*, vol. 40, no. 9, p. 091701, Sep. 2013.

[7] B. Fischl, D. H. Salat, E. Busa, M. Albert, M. Dieterich, C. Haselgrove, A. van der Kouwe, R. Killiany, D. Kennedy, S. Klaveness, A. Montillo, N. Makris, B. Rosen, and A. M. Dale, "Whole brain segmentation: automated labeling of neuroanatomical structures in the human brain." *Neuron*, vol. 33, no. 3, pp. 341–55, Jan. 2002.